# An Orthotopic Lung Tumor Model for Image-Guided Microirradiation in Rats

**Debabrata Saha**[a], **Linda Watkins**[b], **Yi Yin**[b], **Philip Thorpe**[b], **Michael D. Story**[a], **Kwang Song**[a], **Pavithra Raghavan**[a], **Robert Timmerman**[a], **Benjamin Chen**[a], **John D. Minna**[c], and **Timothy D. Solberg**[a],[1]

[a]Department of Radiation Oncology, Division of Molecular Radiation Biology and Simmons Comprehensive Cancer Center, UT Southwestern Medical Center, Dallas, Texas 75390-9187

[b]Department of Pharmacology, UT Southwestern Medical Center, Dallas, Texas 75390-9187

[c]Hamon Center for Therapeutic Oncology Research, UT Southwestern Medical Center, Dallas, Texas 75390-9187

## Abstract

The purpose of this study was to develop a rat orthotopic lung tumor model with a solitary intrapulmonary nodule to study the effects of high-dose radiation. A549-Luc non-small cell lung cancer (NSCLC) cells were implanted into nude rats in the intercostal space between ribs 5 and 6 of the right lung. Bioluminescence and microcomputed tomography (CT) imaging were performed after implantation to confirm the presence of a solitary tumor and to monitor tumor growth. A device using image guidance for localization was developed to facilitate high-precision irradiation in small animals. A pilot irradiation study was performed, and response was assessed by bioluminescence imaging and immunohistochemistry. Radiation response was confirmed through serial bioluminescence imaging, and the strength of the bioluminescence signal was observed to be inversely proportional to dose. Response was also observed by the monoclonal antibody bavituximab, which binds to exposed lipid phosphatidylserine (PS) on tumor vessels. The ability to (1) reproducibly generate solitary tumor nodules in the rat lung, (2) identify and monitor tumor growth by bioluminescence imaging and CT imaging, (3) accurately target these tumors using high doses of radiation, and (4) demonstrate and quantify radiation response using bioluminescence imaging provides significant opportunity to probe the biological mechanisms of high-dose irradiation in preclinical settings.

## INTRODUCTION

Lung cancer is the leading cause for cancer death in the United States; in 2008 it was estimated that approximately 215,000 new lung cancer cases would be diagnosed and that approximately 161,000 people would die from lung cancer (1). Non-small cell lung cancer (NSCLC), consisting of tumors of squamous cell, adenocarcinoma or large cell histologies, comprises 85–90% of all lung cancers. Historically, surgery has been the preferred form of treatment for early-stage NSCLC, resulting in 5-year survival rates of approximately 60 to 70% (2,3). Unfortunately, some patients with NSCLC are unable to tolerate surgery or the postoperative recovery period due to lack of adequate respiratory reserve, cardiac dysfunction, diabetes mellitus, vascular disease, general frailty or other comorbidities.

[1]Address for correspondence: Department of Radiation Oncology, UT Southwestern Medical Center, 2201 Inwood Road, Dallas, TX 75390-9187; Timothy.Solberg@utsouthwestern.edu.

Primary radiation therapy for the early-stage NSCLC is considered a reasonable nonsurgical therapy for these patients, with reported 5-year survival rates ranging from 10–30% (4–10). Improved survival was significantly correlated with local control and approached significance for higher radiation doses ($P = 0.07$) (10). Therefore, it is plausible that superior local control with improved radiation techniques could translate to a survival benefit for medically inoperable NSCLC patients.

Recently, several investigators have explored the use of high-dose focal radiation, conceptually chosen to overcome radiation resistance of the malignant cells, for the treatment of lung tumors. Stereotactic body radiation therapy (SBRT) typically uses doses of up to 28 Gy per fraction, given five or fewer times. This treatment has been applied successfully in brain radiosurgery for over three decades, with excellent local control rates (11,12). Modern techniques, including voxel imaging, 3D dosimetry, and accurate small beam dosimetry, have demonstrated that toxicity can be maintained at acceptable levels with accurate localization. SBRT uses elements of 3D conformal therapy in addition to stereotactic targeting while incorporating a variety of methodologies for decreasing the effects of lung and other organ movement that would otherwise translate into compromised control and/or increased morbidity (13–17). This approach allows dramatic reduction of treatment volumes, facilitating hypofractionation with markedly increased daily doses and significantly reduced overall treatment time. SBRT has been used clinically to treat metastatic and primary tumors in the liver, lung and retroperitoneum with promising results (18–21).

In the first prospective phase I study, 47 patients with medically inoperable NSCLC were treated with radiation doses ranging from 24 to 72 Gy, given in three fractions. In tumors less than 5 cm in size, the dose-limiting toxicity was not reached (22). A follow-on phase II study in 70 patients demonstrated an actuarial 2-year local control of 95% (22). These and other results have led to several national multicenter prospective trials.

The potential for increased normal tissue toxicity is intrinsic to delivery of SBRT. For example, an obvious shortcoming in the implementation of SBRT for lung cancer involves the difficulty in treating central tumors, i.e. a tumor of any T stage within or touching the zone of the proximal bronchial tree. In the initial phase I lung SBRT study, the treatment of tumors within the proximal zone produced an 11-fold increase in toxicity relative to tumors outside the peripheral zone (22). This was largely due to atelectasis occurring downstream from irradiated primary bronchi and bronchioles. For this reason, central tumors were specifically excluded from RTOG 0236, and the dose was reduced significantly in RTOG 0618. In this example, as in the broader range of SBRT applications, the therapeutic ratio may be improved through the addition of agents designed to sensitize the tumor and/or protect normal tissue. This strategy may prove particularly effective when combined with SBRT, because the limited number of fractions in an SBRT schedule may limit the toxicity associated with many response-modifying agents.

To investigate and validate response to SBRT alone or in combination with radiomodulating compounds, it is necessary to develop a tumor model for image-guided high-dose irradiation of rodent tumors and normal tissues in a manner that closely mimics delivery of SBRT in humans. At present, lung is the most targeted clinical site for SBRT; the RTOG has three open lung SBRT trials. For systematic investigation in a preclinical environment, a solitary orthotopic lung tumor model is highly desirable. Current methods for forming solitary intrapulmonary nodules and techniques for delivery of image-guided radiation in such a rodent model are not well developed. In this study, we report on the development of a tumor model in rodent lung and demonstrate successful targeting of lung tumors using image-guided SBRT. To validate image guided delivery of ablative doses in our lung tumor model,

we used a monoclonal antibody that detects anionic phospholipids, primarily phosphatidylserine (PS), that become externalized on tumor endothelial cells in response to radiation (23). The antibody, bavituximab, localizes strongly and specifically to blood vessels in irradiated orthotopic tumors. These findings illustrate how the orthotopic models may enable the design and testing of new strategies for treating NSCLC patients.

## MATERIALS AND METHODS

### Cell Culture

A549-Luc cells provided by Dr. John Minna's laboratory were cultured in RPMI 1640 medium supplemented with 10% FBS in an atmosphere of 95% air/5% $CO_2$ at 37°C. The A549-Luc lung cancer cell line was established using a lentivirus encoding the luciferase gene driven by ubiquitin promoter, and then stable clones were isolated by G418 selection (24).

### Orthotopic Model

A total of $1 \times 10^6$ cells were subsequently mixed with matrigel (1:1) in a final volume of 30 µl. Male nude rats (NIH-RNU, NCI-Frederick, MD) were anesthetized using ketamine (100 mg/ml), xylazine (20 mg/ml), and acepromazine (10 mg/ml) and placed on a rat body frame with the head inclined upward at a 30° angle. Cells were injected in the intercostal space between the ribs 5 and 6 of the right lung using a 28G1/2 needle. A needle guard was used to limit the depth to 0.8 cm beyond the entry point. No skin preparation or shaving was required. After tumor injection, rats were observed for 45–60 min until they had fully recovered. All the experiments were conducted under UTSW Institutional Animal Care and Use Committee-approved guidelines for animal welfare.

### Bioluminescence Imaging

Bioluminescence imaging was performed weekly using an IVIS Lumina Imaging System (Xenogen, Alameda, CA). Rats were anesthetized by 1% isoflurane inhalation followed by an i.p. injection of D-luciferin (stock concentration: 150 mg/ml; 187.5 mg/kg). Bioluminescence images were acquired 10 min after luciferin injection.

### Tissue Sectioning and Immunofluorescence Staining

The monoclonal antibody bavituximab was used to detect exposed PS on tumor vasculature. Bavituximab comprises the Fv regions of the original murine antibody, 3G4 (25), and the constant regions of human IgG1. Bavituximab and 3G4 bind to anionic phospholipids principally on the cell surface, complexed with serum protein β2-glycoprotein 1 (23). The antibody is in clinical trials as a vascular targeting agent for the treatment of cancer. To detect exposed PS, bavituximab (4 mg/kg) was injected i.v. into rats and was allowed to circulate for 4 h. Rats were then anesthetized, exsanguinated and perfused with heparinized saline. Tumors were then removed and snap-frozen, and 5-µm sections were prepared. Tissue sections were fixed and immunostained with different antibodies. Frozen tissue sections were prepared using Leica CM3050S cryostat (Meyer Instrument, Houston, TX). For immunostaining, tissue sections were air dried for 1 h, fixed in 4% paraformaldehyde for 60 min, permeabilized in 0.3% Triton X-100 for 10 min, and then blocked in 5% normal goat serum or 1% bovine serum albumin for 1 h at room temperature. Tissue sections were incubated with primary antibodies for 1 h, washed in PBS, incubated with Alexa-488 and Alexa-568 conjugated secondary antibodies for 30 min (Invitrogen, Carlsbad, CA), washed in PBS, and mounted in Vectashield mounting medium with DAPI (4,6 diamidino-2-phenylindole) (Vector Laboratories, Inc., Burlingame, CA). Fluorescence images were captured using a Zeiss Axiovert 200M microscope equipped with an AxioCam MRm digital

CCD camera. Anti-CD31 was purchased from BD Pharmingen; anti-DNA-PKcs 25-4 mouse monoclonal antibody and anti-Ki67 were purchased from NeoMarkers (Thermo Fisher Scientific, Fremont, CA). The chimeric antibody bavituximab was provided by Peregrine (Tustin, CA). For analysis of DNA double-strand breaks, frozen tissue sections were incubated with primary anti-phospho-Histone (Ser 139) γ-H2AX (Millipore, Billerica, MA) and Rhodamine Red-conjugated goat anti-mouse were used as secondary antibodies (Invitrogen). Tissue sections were then mounted in Vectashield mounting medium containing DAPI for nuclear staining. Phospho-γ-H2AX foci were examined using a Zeiss LSM 510 Meta confocal microscope.

## CT Scans

Animals were followed by weekly bioluminescence imaging, and in those animals demonstrating sufficient luminescence, micro-CT scans were obtained to confirm tumor localization and for subsequent use in treatment planning. Rats were anesthetized using 1% isoflurane inhalation and positioned on the CT bed. Images were obtained through the entire thorax at an isotropic voxel size of 45 µm (80 kV, 450 µA and 400 ms integration time), using the GE eXplore Locus micro-CT scanner (GE HealthCare, Milwaukee, WI). Three-dimensional images were reconstructed from two-dimensional grayscale image slices and visualized using the Microview Software (GE HealthCare).

## Microirradiation

Animals were treated using a dedicated small animal device constructed by our group with capabilities for precision high-dose irradiation. The device is characterized by a high dose rate, small beam size, and accurate and precise target localization facilitated through image guidance. The system has three main components: a collimation mechanism for producing small radiation beams that exhibit a sharp lateral falloff, a digital imaging subsystem, and a two-dimensional positioning stage. The device with individual components labeled is shown in Fig. 1A positioned beneath an X-ray tube and inside an X-RAD 320 irradiator (Precision X-Ray, Inc., North Branford, CT).

The collimation device consists of a 2.5-cm-thick brass alloy disk with interchangeable apertures ranging from 1 to 20 mm in nominal diameter. The actual radiation field is somewhat larger due to geometric magnification and a finite focal spot size. Animal irradiation is performed at 250 kV and 15 mA and with the addition of 1.65 mm aluminum filtration to remove low-energy photons from the beam. Depending on treatment distance and collimator size, this provides dose rates well in excess of 10 Gy/min.

The small animal device is equipped with a PaxScan 1313 amorphous silicon imaging panel (Varian Medical Systems, Palo Alto, CA). Spatial resolution in excess of 4 line pair/mm is adequate for visualizing structures within the rat thorax. Image guidance performed at tube settings of 20 kV and 5 mA provides excellent soft tissue contract. The imaging panel is coupled to an XY positioning stage that is moved under computer control. The height of the stage can be adjusted manually. Image acquisition and positioning are controlled through a MATLAB software application (The Math-Works Inc., Natick, MA) (Fig. 1B). The software has functions for calibrating and centering the imaging panel and positioning stage relative to the radiation beam axis (Fig. 2C).

The process for performing localization and irradiation is shown in Fig. 1D and E. One radio-opaque fiducial marker embedded animal bed is aligned with the beam center. Four radio-opaque fiducial markers are attached to the imaging panel. The initial position of the animal is established using landmarks on the bed, and a localization image is obtained (Fig. 1D). The localization image is compared with reference image, such as a microdigitally

reconstructed radiograph (DRR), to determine the translations needed to position the desired target at the beam center. In this example, the orthotopic tumor is clearly visible on the localization image. The user identifies the desired target location by clicking in the image window (Fig. 1B), and the animal is translated accordingly. After making the necessary shifts, a second image is acquired to verify proper position (Fig. 1E).

## RESULTS

### Development of Rat Orthotopic Model for SBRT

For a systematic study of the effects of SBRT for lung cancer, it is critical to have an orthotopic tumor model that mimics human disease as closely as possible. Ideally, a single tumor nodule should be present in the lung. In our model we sought to establish a single tumor within the middle or the lower lobe of the right lung. Figure 2A shows the dissected specimen and the desired injection site. The injection site was located simply by palpating the animals (Fig. 2B). Figure 2C, E and G shows bioluminescence images of three separate rats three weeks after implantation of A549-Luc cells in the right lung. Figure 2D, F and H show the corresponding single nodule tumor dissected from the lung. This result clearly demonstrates successful orthotopic implantation of human NSCLC cells in the rodent lung, developing into a single tumor nodule. A strong bioluminescence signal was observed on the right side of all animals. Bioluminescence imaging is extremely sensitive; thus if metastasis occurs, it will reveal a diffuse tumor within the animal.

Because of the high inherent contrast between lung and tumor, CT is an excellent modality for targeting lung tumors. Monitoring and triaging animals with CT, however, is not practical. Therefore, it is essential to establish a good correlation between bioluminescence imaging and CT for determination of tumor location and size. Figure 3A shows a clear bioluminescence imaging signal emanating from a tumor in the right lung. The same animal underwent micro-CT imaging, which confirmed a solitary tumor of approximately 7 mm (Fig. 3B, C). To assess metastatic tumor growth outside of the right lung, we injected luciferin i.p. prior to killing the animal. Bioluminescence imaging was then performed in both the intact and dissected animal, confirming that the tumor was confined exclusively to a solid nodule in the right lung (Fig. 3D). The lungs were subsequently dissected from the thorax, and bioluminescence imaging was performed promptly (within 15 min after dissection) on the separated specimen. Again, the residual signal was observed only in the tumor within the right lung (Fig. 3E). Thus all indications demonstrate (1) the presence of a solitary nodule, (2) the absence of metastases, and (3) a strong correlation between the bioluminescence imaging and CT imaging.

### Tumor Response to Image-Guided Irradiation

PS is absent from the surface of blood vessels in normal tissues but becomes exposed on tumor blood vessels in response to oxidative stresses in the tumor microenvironment (26). He *et al.* demonstrated that vascular targeting of human lung tumors by the monoclonal antibody bavituximab was enhanced by ionizing radiation (23). In this study we used the monoclonal antibody bavituximab to identify PS in A549-luc tumors in lungs before and after irradiating the tumors. Figure 4B, panel (ii), shows the increased localization of bavituximab in tumor vessels, indicating that PS becomes exposed (>90%) on tumor endothelium in response to 10 Gy radiation (green). In contrast, about 20% PS exposure and bavituximab localization was observed on the unirradiated tumor tissue [Fig. 4C, panel (ii)]. No bavituximab localization was noted in normal rat lung exposed to 10 Gy radiation [Fig. 4A, panel (ii)]. To confirm tumor vasculature labeling by bavituximab, vascular endothelium was stained with a mouse anti-rat CD31 antibody [Fig. 4A–C, panel (i)]. Nuclei were stained with DAPI [blue, Fig. 4A–C, panel (iii)]. Figure 4B, panel (iv), shows that the

merged image of the tumor vessel is yellow. No convergent staining was visible in either the irradiated normal lung tissue [Fig. 4A, panel (iv)] or unirradiated tumor tissue [Fig. 4C, panel (iv)]. Thus radiation exposure induces PS strongly and selectively on the tumor vessel. In an additional experiment, we also performed γ-H2AX staining to detect DNA double-strand breaks postirradiation in the same tumor sample. An early step in DSB repair involves the rapid phosphorylation of γ-H2AX that forms foci at the damage sites (27,28). A serial tissue section was prepared from the same irradiated lung tumor used for PS staining subjected to phospho-γ-H2AX staining (red) while DAPI (blue) was used for nuclear staining (Fig. 4D). Significant numbers of DNA double-strand breaks were still visible 24 h postirradiation (Fig. 4D, lower panel). For the unirradiated sample, a rat bearing a similar orthotopic lung tumor was killed. Tissue sections subjected to phospho-γ-H2AX and DAPI staining (Fig. 4D, upper panel) showed no evidence of DNA double-strand breaks.

It is essential to distinguish the tumor region from the stromal microenvironment while evaluating the immediate and the long-term effects of SBRT. To this end, differentiation of tumor from the surrounding normal lung tissue was performed by immunohistochemical analysis. Frozen lung tissue sections were incubated with monoclonal anti-DNA-PKcs antibody (25-4, recognizing only human DNA-PKcs but not murine DNA-PKcs) and/or anti-Ki67 antibody for cell proliferation. The results clearly showed that DNA-PKcs staining occurred primarily in the tumor region (Fig. 4E) but not in the normal rat lung tissues, since these antibodies are human specific. We also observed that the extent of Ki67 staining was higher in the tumor regions that were stained positive with DNA-PKcs (Fig. 4F). Furthermore, Ki67 staining also revealed the distinct morphology of cells of human origin with slightly larger nuclei than these of cells rat origin in the adjacent normal lung tissues (Fig. 4E–G).

A549-Luc tumor cells were injected into the lungs of two rats, and tumor growth was then monitored by routine bioluminescence imaging. Image-guided radiation treatment was initiated when the bioluminescence signal (integrated over an appropriate region of interest) reached approximately $1 \times 10^6 - 1 \times 10^7$ photons/s/cm$^2$/sr. One animal received a total dose of 60 Gy in three fractions on days 20, 45 and 59 as indicated (Fig. 5B). The animal was followed closely with bioluminescence imaging, and when tumor growth was observed, an additional dose was administered. While a complete bioluminescence imaging response was not observed, the tumor volume remained stable, with an integrated bioluminescence imaging signal of approximately $2.5 \times 10^7$ p/s/cm$^2$/sr, over a period of nearly 4 months. No treatment-related toxicity was observed in this animal. In contrast, the untreated animal experienced uncontrolled tumor growth, with an integrated bioluminescence imaging signal of $4 \times 10^9$ p/s/cm$^2$/sr on day 41. It is important to note that the orthotopic tumors grow at different rates after implantation; at the time of the first bioluminescence imaging session (time = 0 in Fig. 5C), the tumor burden in the untreated animal was significantly higher than that of the animal eventually treated. Therefore, bioluminescence imaging is an essential tool for monitoring tumor growth to determine the optimal treatment time.

Our data clearly demonstrate that A549 tumors are highly aggressive in the lungs of nude rats and are difficult to control if not treated at an early stage (Fig. 5A). After a total dose of 60 Gy was delivered, complete tumor ablation was not achieved. This can attributed to the intrinsic radioresistance property of the A549 cells, consistent with data from clonogenic assays (29,30) as well as with the gap between fractions.

## DISCUSSION

For almost two decades, human lung cancer xenografts have been established in the lungs of immunodeficient rodents. Because of the anatomical location and microenvironment

surrounding the tumor, these models have been very helpful in evaluating cancer therapies. These models were further improved after genetic manipulation of a reporter luciferase gene in the human cancer cell genome, providing a mechanism for monitoring tumor progression and response using bioluminescence imaging. However, the stringent requirement of an appropriate orthotopic lung tumor model for stereotactic body radiation therapy, in which an ablative radiation dose can be administered to the tumor while minimizing normal lung toxicity, required the ability to reproducibly produce a solitary nodule within a desired location in the lung. Current orthotopic lung models, developed primarily in mice, are inappropriate for this application due to widespread dissemination of tumors growing in both lungs. Additionally, the small size of the mouse lung precludes delivery of large doses without excessive morbidity. Our studies demonstrate that a single tumor can be introduced into a specific location in the rat lung and treated effectively with high radiation doses without dose-limiting toxicity.

Several models describing the formation of orthotopic lung tumors have been reported. Yamaura *et al.* developed a model for mediastinal lymph node metastasis in the C57/BL6 mouse by implantation of Lewis lung carcinoma cells in the intercostal space (31). Onn *et al.* developed an orthotopic lung model in nude mice to study the efficacy of chemotherapeutic drugs (32). Injection of tumor cells in saline was quickly followed by diffuse dissemination. Cells suspended in matrigel initially produced a solitary lesion, which then spread progressively within animals. March *et al.* described a rat orthotopic lung model in which NSCLC cells with EDTA or elastase were implanted surgically through the trachea (33). They observed that co-administration of tumor cells with EDTA significantly enhanced the tumor uptake rate but was also associated with the rapid development of multiple tumors within the lung (33). An intrabronchial instillation approach to develop a rat lung cancer was also described by Byhardt *et al.* (34).

Like Onn *et al.*, our model requires no surgical intervention. Serial bioluminescence imaging provides an excellent mechanism for tracking tumor development over several weeks until tumor characteristics are suitable for therapy. Based on bioluminescence imaging, our success rate in developing a solitary tumor is essentially 100%. However, on subsequent CT and dissection, this rate falls to 60%. The two common sources of failure are injection at the wrong level, either too superior or too inferior, and failure to insert the needle to the appropriate depth. The latter produces multiple disease foci, which is suboptimal for stereotactic irradiation. To improve our success rate, we are now developing a technique for image-guided tumor cell implantation. This will enable us to visualize the precise needle location prior to injection of the matrigel mixture.

Since the end point of this study is either complete ablation or long-term control of tumor growth, noninvasive monitoring of tumor progression before and after therapeutic interventions is necessary. Bioluminescence imaging is based on oxidation of substrate D-luciferin by luciferase in the presence of $O_2$ and ATP resulting in the emission of light (35). The comparison of bioluminescence imaging with other imaging modalities including CT and MRI has been reported (36). In this study we used both bioluminescence imaging and CT for identification, localization and targeting of SBRT delivery. We demonstrated that bioluminescence imaging and CT are necessary for successful SBRT as well as for verifying response to therapy (Fig. 5). Additionally, the response was validated in irradiated tumors by demonstrating the localization of bavituximab to PS that becomes exposed on tumor vascular endothelium after irradiation (23). With the success of this model, a number of further studies are anticipated.

One shortcoming of our current irradiation system is the inability to easily focus beams from multiple directions. We are presently developing a rotational stage to facilitate multibeam

delivery. Nevertheless, we believe the physical limitation does not present any biological limitations; that is, all of the relevant biology can be probed and peripheral toxicity minimized, even without the efficient multibeam capability.

## Acknowledgments

## REFERENCES

1. Ries, LAG.; Melbert, D.; Krapcho, M.; Stinchcomb, DG.; Howlader, N.; Horner, MJ.; Mariotto, A.; Miller, BA.; Feuer, EJ.; Edwards, BK., editors. SEER Cancer Statistics Review, 1975–2005. Bethesda, MD: National Cancer Institute; 2008. http://seer.cancer.gov/csr/1975_2005/, based on November 2007 SEER data submission, posted to the SEER website

2. Flehinger BJ, Kimmel M, Melamed MR. The effect of surgical treatment on survival from early lung cancer. Implications for screening. Chest 1992;101:1013–1018. [PubMed: 1313349]

3. Gale NW, Yancopoulos GD. Growth factors acting via endothelial cell-specific receptor tyrosine kinases: VEGFs, angiopoietins, and ephrins in vascular development. Genes Dev 1999;13:1055–1066. [PubMed: 10323857]

4. Armstrong JG, Minsky BD. Radiation therapy for medically inoperable stage I and II non-small cell lung cancer. Cancer Treat. Rev 1989;16:247–255. [PubMed: 2561593]

5. Coy P, Kennelly GM. The role of curative radiotherapy in the treatment of lung cancer. Cancer 1980;45:698–702. [PubMed: 6244073]

6. Dosoretz DE, Katin MJ, Blitzer PH, Rubenstein JH, Galmarini DH, Garton GR, Salenius SA. Medically inoperable lung carcinoma: the role of radiation therapy. Semin. Radiat. Oncol 1996;6:98–104. [PubMed: 10717168]

7. Dosoretz DE, Katin MJ, Blitzer PH, Rubenstein JH, Salenius S, Rashid M, Dosani RA, Mestas G, Siegel AD, Chadha TT. Radiation therapy in the management of medically inoperable carcinoma of the lung: results and implications for future treatment strategies. Int. J. Radiat. Oncol. Biol. Phys 1992;24:3–9. [PubMed: 1324899]

8. Haffty BG, Goldberg NB, Gerstley J, Fischer DB, Peschel RE. Results of radical radiation therapy in clinical stage I, technically operable non-small cell lung cancer. Int. J. Radiat. Oncol. Biol. Phys 1988;15:69–73. [PubMed: 2839443]

9. Kaskowitz L, Graham MV, Emami B, Halverson KJ, Rush C. Radiation therapy alone for stage I non-small cell lung cancer. Int. J. Radiat. Oncol. Biol. Phys 1993;27:517–523. [PubMed: 8226143]

10. Sibley GS, Jamieson TA, Marks LB, Anscher MS, Prosnitz LR. Radiotherapy alone for medically inoperable stage I non-small-cell lung cancer: the Duke experience. Int. J. Radiat. Oncol. Biol. Phys 1998;40:149–154. [PubMed: 9422571]

11. Pirzkall A, Debus J, Lohr F, Fuss M, Rhein B, Engenhart-Cabillic R, Wannenmacher M. Radiosurgery alone or in combination with whole-brain radiotherapy for brain metastases. J. Clin. Oncol 1998;16:3563–3569. [PubMed: 9817276]

12. Varlotto JM, Flickinger JC, Niranjan A, Bhatnagar AK, Kondziolka D, Lunsford LD. Analysis of tumor control and toxicity in patients who have survived at least one year after radiosurgery for brain metastases. Int. J. Radiat. Oncol. Biol. Phys 2003;57:452–464. [PubMed: 12957257]

13. Herfarth KK, Debus J, Lohr F, Bahner ML, Fritz P, Hoss A, Schlegel W, Wannenmacher MF. Extracranial stereotactic radiation therapy: set-up accuracy of patients treated for liver metastases. Int. J. Radiat. Oncol. Biol. Phys 2000;46:329–335. [PubMed: 10661339]

14. Lax I, Blomgren H, Naslund I, Svanstrom R. Stereotactic radiotherapy of malignancies in the abdomen. Methodological aspects. Acta Oncol 1994;33:677–683. [PubMed: 7946448]

15. Papiez L, Timmerman R, DesRosiers C, Randall M. Extracranial stereotactic radioablation: physical principles. Acta Oncol 2003;42:882–894. [PubMed: 14968949]

16. Uematsu M, Sonderegger M, Shioda A, Tahara K, Fukui T, Hama Y, Kojima T, Wong JR, Kusano S. Daily positioning accuracy of frameless stereotactic radiation therapy with a fusion of computed tomography and linear accelerator (focal) unit: evaluation of z-axis with a z-marker. Radiother. Oncol 1999;50:337–339. [PubMed: 10392820]

17. Wulf J, Haedinger U, Oppitz U, Thiele W, Mueller G, Flentje M. Stereotactic radiotherapy for primary lung cancer and pulmonary metastases: A noninvasive treatment approach in medically inoperable patients. Int. J. Radiat. Oncol. Biol. Phys 2004;60:186–196. [PubMed: 15337555]

18. Blomgren H, Lax I, Naslund I, Svanstrom R. Stereotactic high dose fraction radiation therapy of extracranial tumors using an accelerator. Clinical experience of the first thirty-one patients. Acta Oncol 1995;34:861–870. [PubMed: 7576756]

19. Herfarth KK, Debus J, Lohr F, Bahner ML, Rhein B, Fritz P, Hoss A, Schlegel W, Wannenmacher MF. Stereotactic single-dose radiation therapy of liver tumors: results of a phase I/II trial. J. Clin. Oncol 2001;19:164–170. [PubMed: 11134209]

20. Timmerman RD, Forster KM, Chinsoo Cho L. Extracranial stereotactic radiation delivery. Semin. Radiat. Oncol 2005;15:202–207. [PubMed: 15983945]

21. Timmerman RD, Kavanagh BD. Stereotactic body radiation therapy. Curr. Probl. Cancer 2005;29:120–157. [PubMed: 16059851]

22. Timmerman RD, Park C, Kavanagh BD. The North American experience with stereotactic body radiation therapy in non-small cell lung cancer. J. Thorac. Oncol 2007;2:S101–S112. [PubMed: 17603304]

23. He J, Luster TA, Thorpe PE. Radiation-enhanced vascular targeting of human lung cancers in mice with a monoclonal antibody that binds anionic phospholipids. Clin. Cancer Res 2007;13:5211–5218. [PubMed: 17785577]

24. Dikmen ZG, Gellert GC, Jackson S, Gryaznov S, Tressler R, Dogan P, Wright WE, Shay JW. *In vivo* inhibition of lung cancer by GRN163L: a novel human telomerase inhibitor. Cancer Res 2005;65:7866–7873. [PubMed: 16140956]

25. Ran S, Thorpe PE. Phosphatidylserine is a marker of tumor vasculature and a potential target for cancer imaging and therapy. Int. J. Radiat. Oncol. Biol. Phys 2002;54:1479–1484. [PubMed: 12459374]

26. Marconescu A, Thorpe PE. Coincident exposure of phosphatidylethanolamine and anionic phospholipids on the surface of irradiated cells. Biochim. Biophys. Acta 2008;1778:2217–2224. [PubMed: 18570887]

27. Burma S, Chen BP, Murphy M, Kurimasa A, Chen DJ. ATM phosphorylates histone H2AX in response to DNA double-strand breaks. J. Biol. Chem 2001;276:42462–42467. [PubMed: 11571274]

28. Kobayashi J, Tauchi H, Chen B, Burma S, Tashiro S, Matsuura S, Tanimoto K, Chen DJ, Komatsu K. Histone H2AX participates the DNA damage-induced ATM activation through interaction with NBS1. Biochem. Biophys. Res. Commun 2009;380:752–757. [PubMed: 19338747]

29. Das AK, Sato M, Story MD, Peyton M, Graves R, Redpath S, Girard L, Gazdar AF, Shay JW, Nirodi CS. Non-small-cell lung cancers with kinase domain mutations in the epidermal growth factor receptor are sensitive to ionizing radiation. Cancer Res 2006;66:9601–9608. [PubMed: 17018617]

30. Kodym E, Kodym R, Reis AE, Habib AA, Story MD, Saha D. The small-molecule CDK inhibitor, SNS-032, enhances cellular radiosensitivity in quiescent and hypoxic non-small cell lung cancer cells. Lung Cancer 2009;66:37–47. [PubMed: 19193471]

31. Yamaura T, Doki Y, Murakami K, Saiki I. Model for mediastinal lymph node metastasis produced by orthotopic intrapulmonary implantation of lung cancer cells in mice. Hum. Cell 1999;12:197–204. [PubMed: 10834106]

32. Onn A, Isobe T, Itasaka S, Wu W, O'Reilly MS, Ki Hong W, Fidler IJ, Herbst RS. Development of an orthotopic model to study the biology and therapy of primary human lung cancer in nude mice. Clin. Cancer Res 2003;9:5532–5539. [PubMed: 14654533]

33. March TH, Marron-Terada PG, Belinsky SA. Refinement of an orthotopic lung cancer model in the nude rat. Vet. Pathol 2001;38:483–490. [PubMed: 11572555]

34. Byhardt RW, Almagro UA, Fish BL, Moulder JE. Development of a rat lung cancer model. Int. J. Radiat. Oncol. Biol. Phys 1984;10:2125–2130. [PubMed: 6490438]

35. McElroy WD. Properties of the reaction utilizing adenosinetriphosphate for bioluminescence. J. Biol. Chem 1951;191:547–557. [PubMed: 14861201]

36. Szentirmai O, Baker CH, Lin N, Szucs S, Takahashi M, Kiryu S, Kung AL, Mulligan RC, Carter BS. Noninvasive bioluminescence imaging of luciferase expressing intracranial U87 xenografts: correlation with magnetic resonance imaging determined tumor volume and longitudinal use in assessing tumor growth and antiangiogenic treatment effect. Neurosurgery 2006;58:365–372. [PubMed: 16462491]
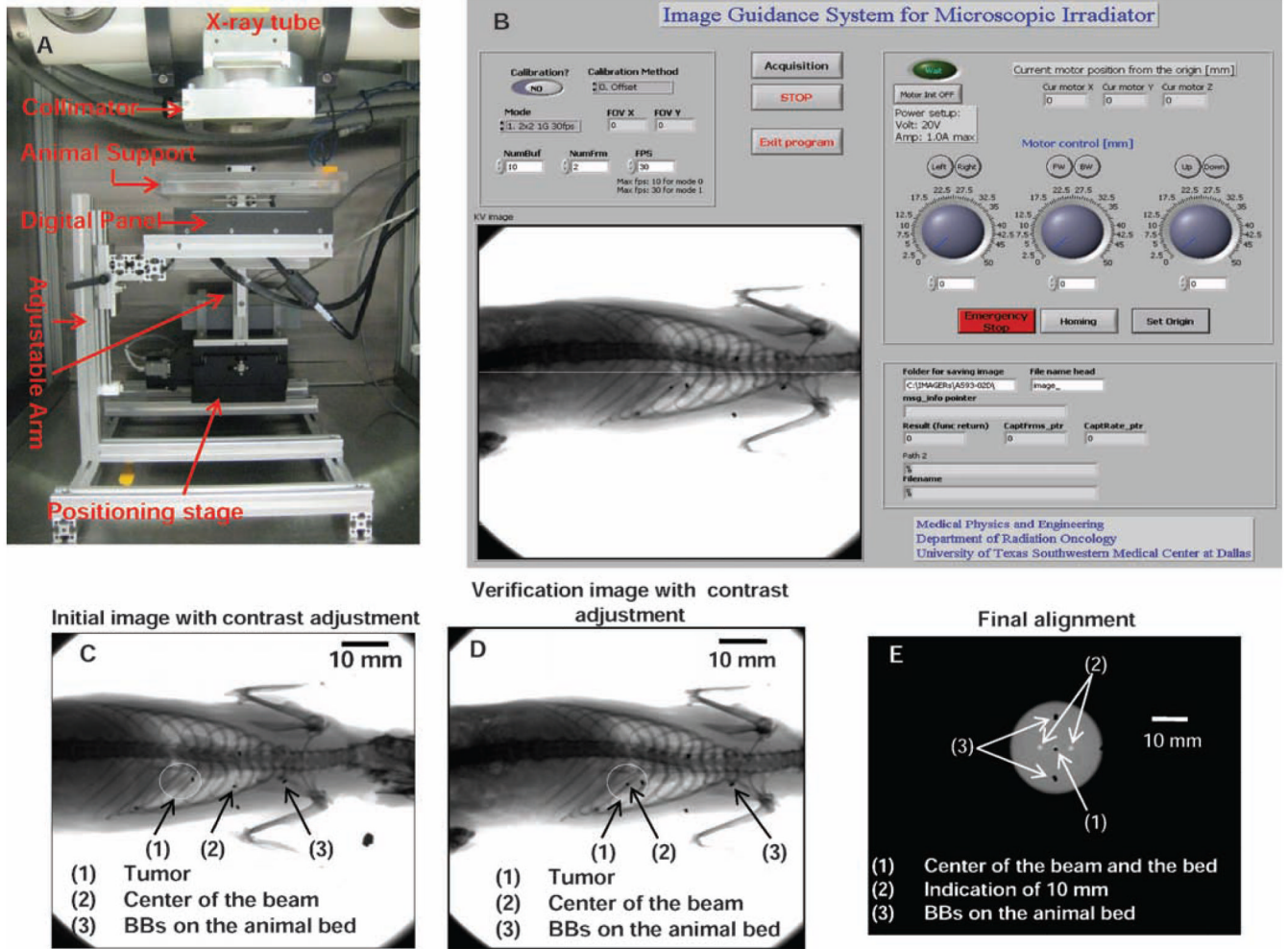
**FIG. 1.**
The image-guided small animal irradiation device (panel A) with major components indicated, positioned beneath a commercial X-ray source. Panel B: Software for image acquisition and positioning. Panel C: Initial localization image with beam center and tumor indicated. Panel D: Final localization verified by a second image. Panel E: Calibration and centering relative to the beam axis.
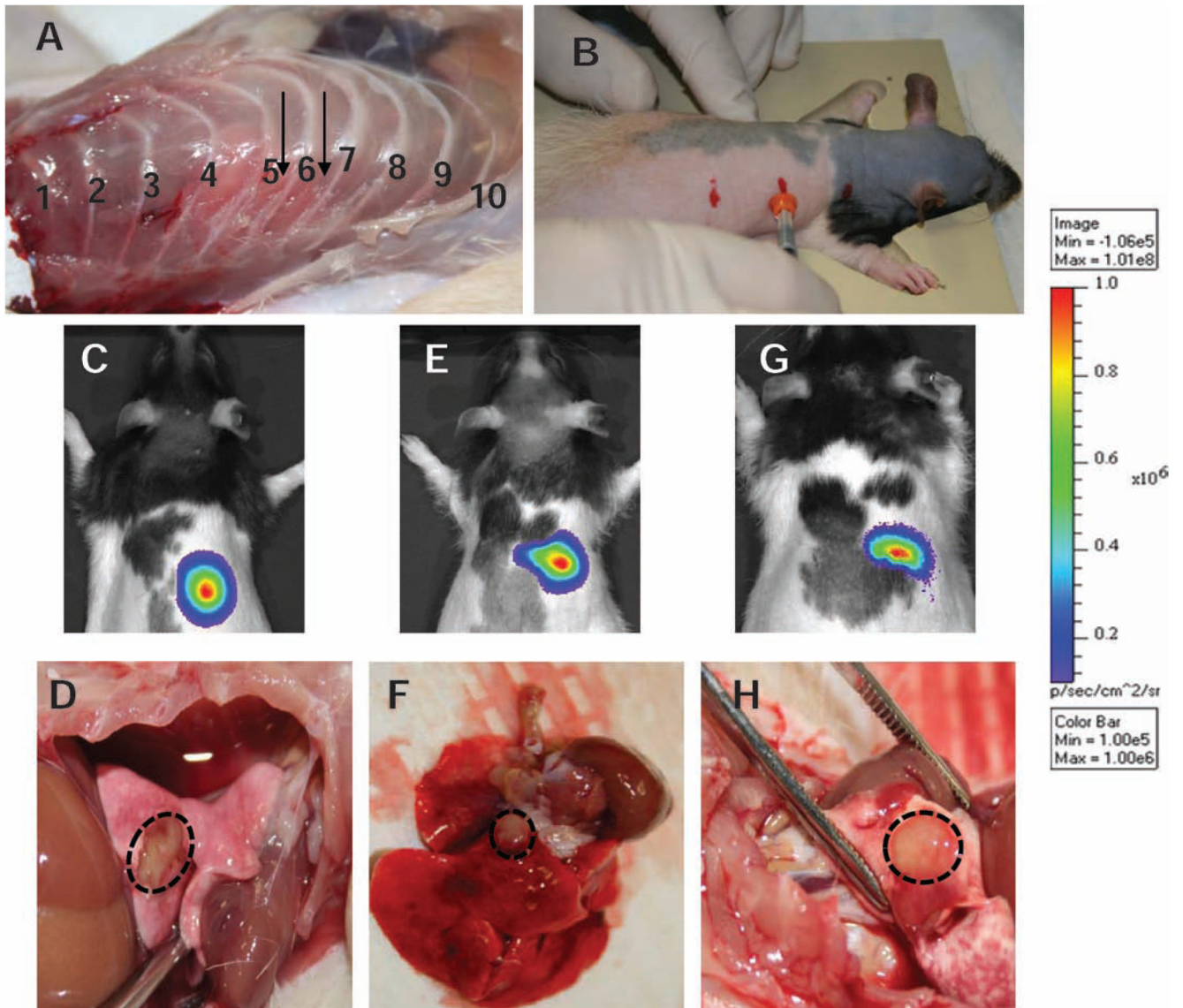
**FIG. 2.**
Development of rat orthotopic model for SBRT. Panel A: Dissected specimen showing the desired injection site. Panel B: Rats are anesthetized using rat cocktail and placed on a supporting frame head up inclined at 30° angle. The upper, middle and bottom marks indicate ribs 1, 6 and 12, respectively. Cells mixed with matrigel are implanted using a 28G1/2 needle. A needle guard is used to control the depth. Panels C, E and G: Bioluminescence imaging in three animals 3 weeks after implantation. Panels D, F and H: Corresponding high-resolution digital image of the solitary nodule in the rat lung.
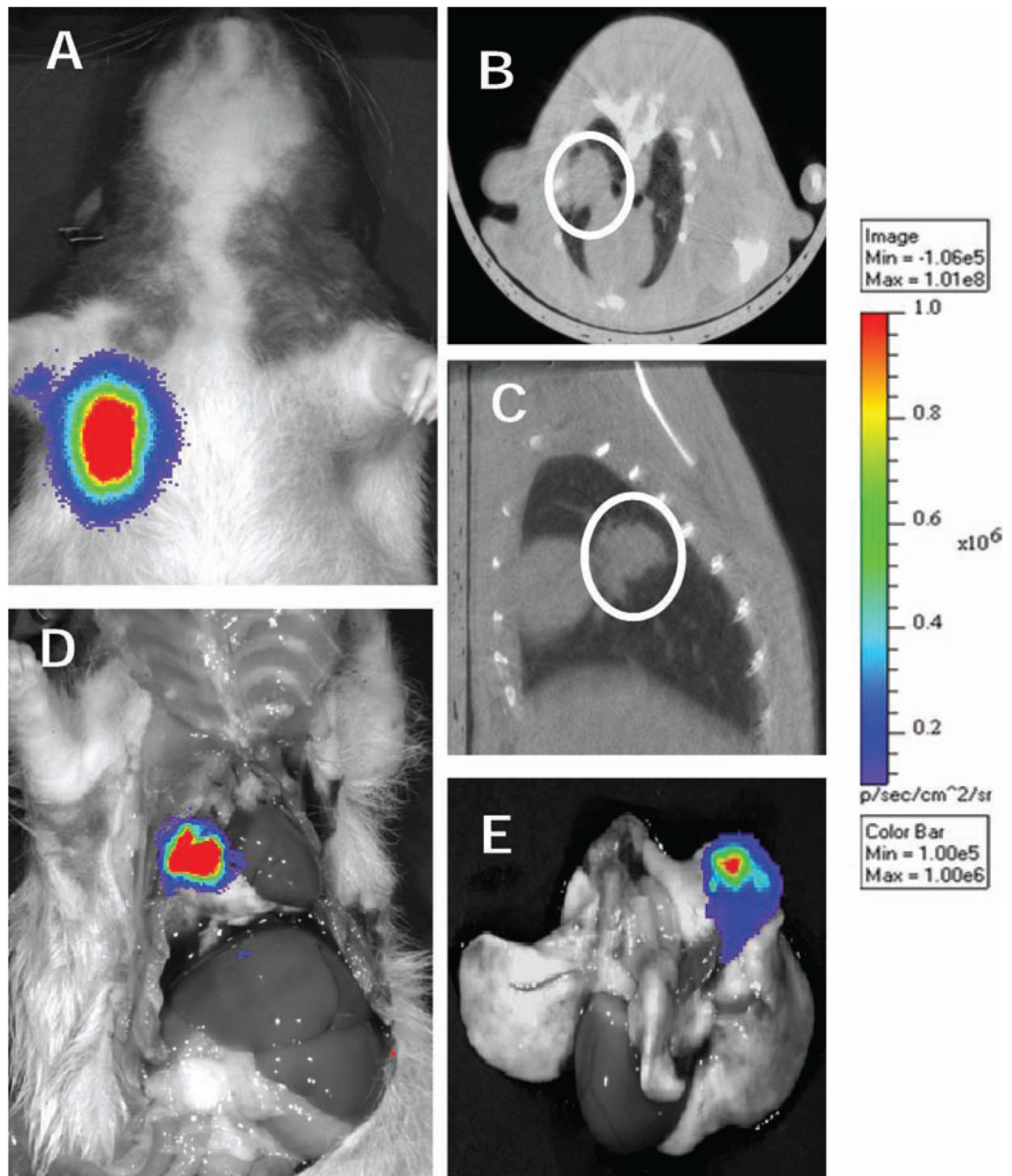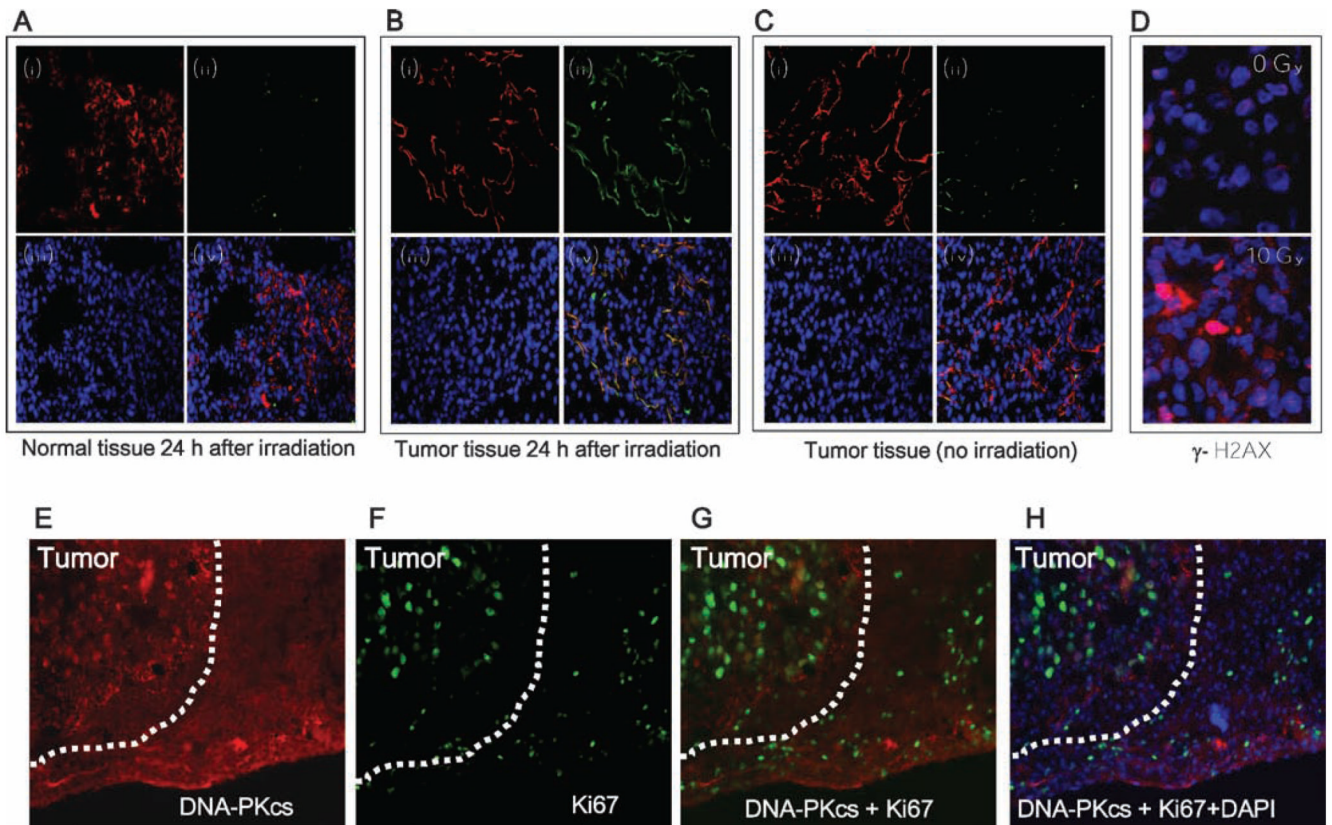
**FIG. 3.**
Panel A: Bioluminescence signal 3 weeks after implantation. Panel B: Micro-CT coronal view, panel C: Micro-CT axial view, and panel D: bioluminescence imaging of the same animal after dissection. Panel E: Bioluminescence imaging of the dissected lung.

**FIG. 4.**
Target validation after Image-guided radiation. Panel A: Normal lung tissue harvested 24 h after irradiation; panel B: tumor tissue harvested 24 h after irradiation; panel C: Unirradiated tumor tissue. In all panels: (i) vascular endothelium detected by mouse anti-rat CD31 antibody followed by Cy3-goat anti-mouse antibody (red), (ii) bavituximab detected using biotinylated goat anti-human IgG followed by Cy2-streptavidin (green), (iii) DNA detected by DAPI (blue), (iv) CD31, bavituximab, and DNA merge image. Panel D: Tumor immunofluorescence staining; merged image of DAPI and phospho-γ-H2AX (0 Gy, upper panel) and irradiated tumors (10 Gy, lower panel). Panel E: DNA-PKcs; panel F: Ki67; panel G, DNA-PKcs and Ki67 merge image; panel H: DNA-PKcs, Ki67 and DAPI merge image.
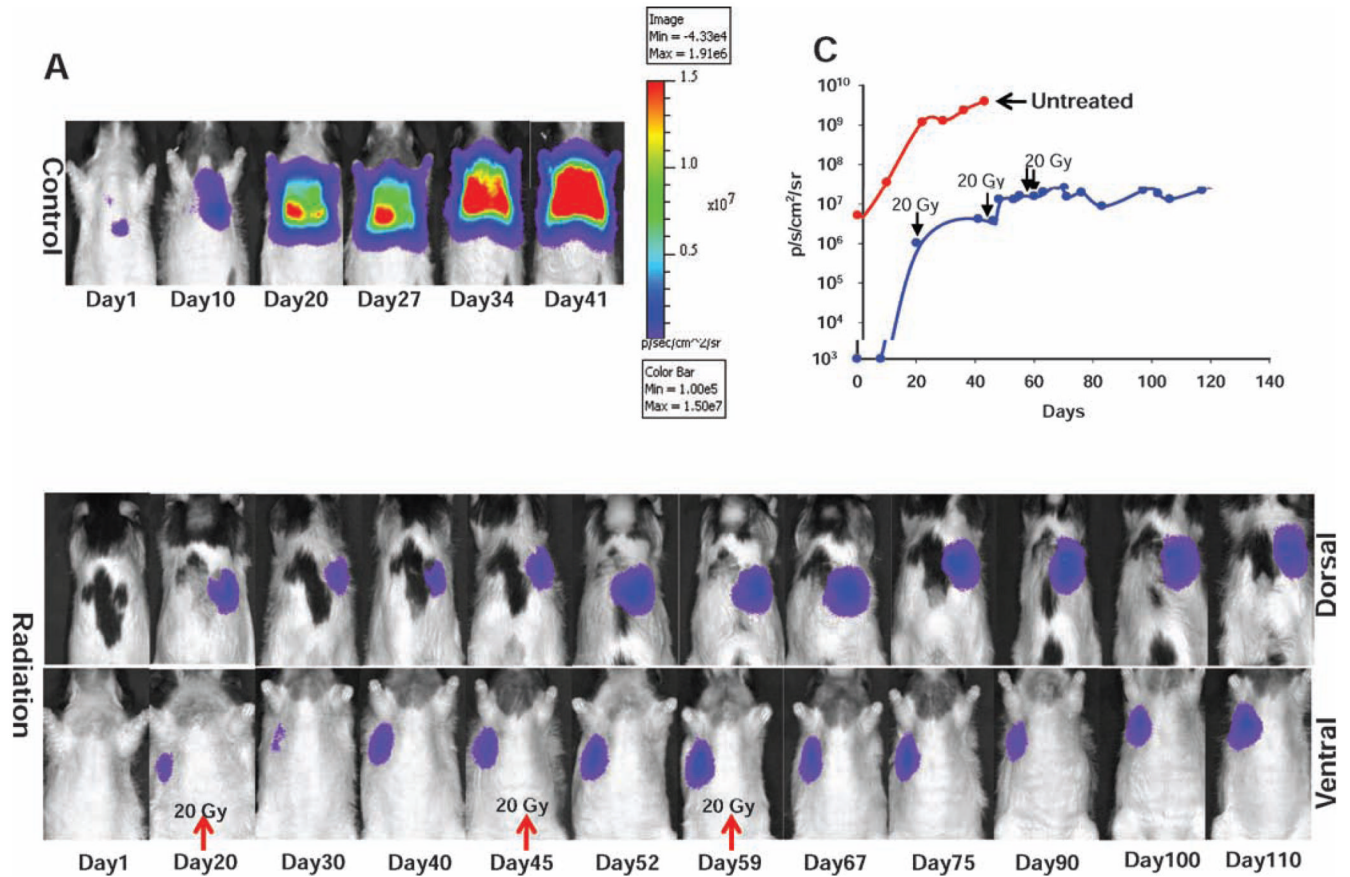
**FIG. 5.**
Tumor progression after (panel A) no treatment and (panel B) delivery of 60 Gy in three fractions on days 20, 45 and 59. The heat scale is given in signal intensity per unit area. Panel C: Tumor growth curve obtained by integrating the bioluminescence imaging signal over a region of interest.